Curved Kirigami SILICOMB cellular structures with zero Poisson's ratio for large deformations and morphing

Yijin Chen[1,2], Fabrizio Scarpa[2], Chrystel Remillat[2,3], Ian Farrow[2], Yanju Liu[4] and Jinsong Leng[1]

Abstract
The work describes the design, manufacturing, and parametric modeling of a curved cellular structure (SILICOMB) with zero Poisson's ratio produced using Kirigami techniques from polyetheretherketone films. The large deformation behavior of the cellular structure is evaluated using full-scale finite element methods and experimental tests performed on the cellular samples. Good agreement is observed between the mechanical behavior predicted by the finite element modeling and the three-point bending compression tests. Finite element simulations have also been used to perform a parametric analysis of the stiffness against the geometry of the cellular structures, showing a high degree of tailoring that these cellular structures could offer in terms of minimum relative density and maximum stiffness. The experimental results also show high levels of strain-dependent loss factors and low residual deformations after cyclic large deformation loading.

Keywords
Cellular structures, zero Poisson's ratio, finite element, loss factor, stiffness, morphing

Introduction

During the last decades, cellular and lattice structures have attracted significant attention from researchers within the mechanics of solids community due to their significant lightweight and out-of-plane stiffness properties (Bitzer, 1997). Cellular solids have been widely developed and used as sandwich cores in a variety of engineering applications, ranging from marine to aerospace and automotive lightweight constructions (Alderson et al., 2010a, 2010b). The conventional hexagonal honeycomb is a typical example of a cellular core configuration, with unit cells made of ribs with equal length and an internal cell angle of 30° (Gibson and Ashby, 1997). Overexpanded centersymmetric honeycombs with special orthotropic properties can also be developed when varying the cell wall aspect ratio and internal cell angle, always with positive values (Bezazi et al., 2005; Gibson and Ashby, 1997). Hexagonal honeycombs with convex configuration (i.e. positive internal cell angle leading to positive Poisson's ratio (PPR)) exhibit anticlastic or saddle-shaped curvatures when subject to out-of-plane bending (Evans, 1991; Lakes, 1987; Masters and Evans, 1996). On the contrary, if the in-plane Poisson's ratios of the cellular structures are negative (i.e. auxetic, or NPR), the curvature is synclastic, with a resulting dome-shaped configuration (Evans and Alderson, 2000a; Lakes, 1987; Miller et al., 2010). In comparison with conventional cellular structures, the auxetic cellular configurations feature increased in-plane shear modulus and enhanced indentation resistance (Evans, 1991; Evans and Alderson, 2000b; Lakes, 1987; Milton, 1992). Auxetic cellular structures have also been used to prototype morphing wings (Bettini et al., 2010; Bornengo et al., 2005; Martin et al., 2008; Spadoni et al., 2006), radomes (Scarpa et al., 2003), adaptive, and deployable

[1]Centre for Composite Materials and Structures, Science Park of Harbin Institute of Technology (HIT), China
[2]Advanced Composites Centre for Innovation and Science, University of Bristol, UK
[3]Aerospace Engineering, University of Bristol, UK
[4]Department of Aerospace Science and Mechanics, Harbin Institute of Technology (HIT), China

Corresponding author:
Fabrizio Scarpa, Advanced Composites Centre for Innovation and Science, University of Bristol, Bristol BS8 1TR, UK.
Email: f.scarpa@bristol.ac.uk
Jinsong Leng, Centre for Composite Materials and Structures, Science Park of Harbin Institute of Technology (HIT), No. 2 YiKuang Street, P.O. Box 3011, Harbin 150080, China.
Email: lengjs@hit.edu.cn

structures (Hassan et al., 2008). Both types of honeycombs can be used as the core of sandwich composites, but it is difficult to be use them in morphing cylindrical applications (Grima et al., 2010). In that sense, cellular structures with zero Poisson's ratio (ZPR) do not produce anticlastic and synclastic curvature behaviors, but can be used to manufacture cores for tubular structures (Grima et al., 2010), such as air intakes.

ZPR also implies that the solid does not deform laterally when subjected to mechanical loading (tensile or compressive) (Lira et al., 2011). In the field of morphing skins, a candidate solution proposed by some authors is sandwich cellular cores with flexible face sheets (Bubert et al., 2010; Olympio and Gandhi, 2007, 2010a). For one-dimensional (1D) morphing applications, the confinement of the lateral deformation belonging to cellular structures (with PPR and NPR) will result in a substantial increase in the effective modulus along the morphing direction (Olympio and Gandhi, 2007, 2010b). To solve this problem, Olympio and Gandhi (2010a, 2010b) and Bubert et al. (2010) have proposed the use of ZPR cellular structures for cores to be used in 1D morphing skins. Another application of ZPR cellular structures has been previously identified by Engelmayr et al. (2008), who demonstrated the feasibility of using accordion-like honeycomb microstructures as scaffolds with controllable stiffness and anisotropy for myocardial tissue engineering. Grima et al. (2010) have recently evaluated a new ZPR cellular structure based on a semi reentrant honeycomb configuration. Another contribution to the field of ZPR cellular structures is the SILICOMB configuration developed by Lira et al. (2009, 2011), which is inspired by the amorphous silica lattice geometry and can be considered a generalization of the accordion honeycomb concept (Olympio and Gandhi, 2007). Much of the previous work cited has focused on the mechanical behavior of planar cellular configurations. However, less significant amount of work has been dedicated to tubular or curved cellular structures. Jeong and Ruzzene (2004) have investigated the wave propagation behavior in cylindrical grid-like structures with hexagonal and reentrant shape leading to NPR effect. Scarpa et al. (2008) have investigated the variation of axial stiffness, radial Poisson's ratio, and buckling behavior of tubular configurations with reentrant unit cell shape. However, to the best of the authors' knowledge, no specific work has been done on curved cellular configurations with nontubular layout. Moreover, no investigation has been reported so far on curved cellular structures with ZPR behavior.

This work is mainly concerned with the stiffness exhibited by various curved SILICOMB configurations using with finite element (FE) simulations and experimental methods. A full-scale curved SILICOMB topology is simulated using FE analysis, with boundary conditions representing experimental compression tests.

The curved cellular honeycomb samples with ZPR have been manufactured using Kirigami techniques applied to thermoplastics (polyetheretherketone (PEEK)). Kirigami is a manufacturing method combining Origami (ply-folding procedures) together with cut patterns and is particularly suited to produce composite cellular structures with complex tessellations and geometry, such as a morphing wingbox concept developed by some of the researchers (Saito et al., 2011). Curved SILICOMB PEEK cellular structures are currently evaluated as possible cores in sandwich reflectors, due to the low thermal capacity, high-temperature performance, and good mechanical behavior of thermoplastics PEEK. The experimental results have been used to benchmark the FE model and perform a parametric analysis of the stiffness of the curved SILICOMB configurations versus the geometry parameters defining the unit cell of the ZPR structure. The compressive tests also show the capability of the curved cellular configuration to undergo large deformations and recover the initial shape, as well as providing large hysteresis under cyclic loading at low strain rate levels.

Geometry and model

Geometry

Figure 1 shows the geometric parameters of the curved SILICOMB unit configuration. The representative unit cell (within the black dotted line) is composed by two walls (L and H) with thickness t, depth b, and defined by two internal angles (ϕ and θ). For convenience, three nondimensional parameters $\alpha = H/L$, $\beta = t/L$, and $\gamma = b/L$ are defined as the aspect, thickness, and depth ratios of the cell wall, respectively. The geometry layout of the unit cell can be changed according to the parameter selection for the angles ϕ and θ. For an internal cell angle of $\phi = 0$, the SILICOMB configuration reduces to the accordion honeycomb structure.

FE simulation

The mechanical behavior of the curved SILICOMB cellular structures has been simulated using the commercial FE analysis package (ANSYS, version 11.0, Ansys, Inc.). Full-scale FE models have been prepared using four-node element SHELL181 with three translation degrees of freedom (DOF) along the x-, y-, and z-directions, and three rotational DOFs around the x-, y-, and z-axes. This element is also well suited for linear, and large rotation, and/or large strain nonlinear applications. The simulations were performed on a full-scale volume model of 3.5×4 cells with an average mesh size of $L/5$ (Figure 2), representative of the samples manufactured using the Kirigami technique. A total of 8960 elements have been used to construct the model. The deformation of the curved cellular sample
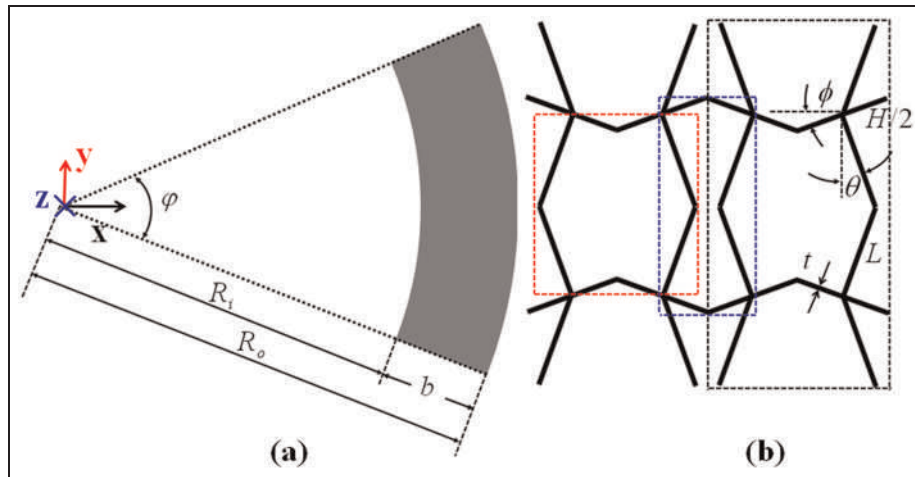
Figure 1. Geometry parameters defining the unit cells: internal cell angles ϕ, φ, θ, ribs lengths H and L, radiuses R_i and R_o, width b and thickness t.

subjected to central loading was simulated initially using a linear FE approach. To investigate from a numerical point of view the energy absorption capability and the damping properties, a series of quasi-static nonlinear analysis (with Newton–Raphson algorithms) and nonlinear transient analysis (with full method) were used to simulate the force–displacement behavior under the loading and unloading cycles. Contact pairs were created between the peak nodes of inside strips and the surface of the adjacent strips to prevent element penetration during the simulations (Figure 3). The CONTA 175 element was used to model the contact elements (the peak nodes of the strips), while the TARGE 170 elements were representing the surfaces of the adjacent strips. The nonlinear and transient dynamics simulations were controlled using the STABILIZE command. To activate the command, an energy dissipation ratio of 0.2 obtained from the experimental test results was used in both types of the nonlinear FE models. According to the data sheet provided by the supplier, the PEEK material shows an isotropic mechanical behavior ($E_c = 1.8$ GPa, $\nu_c = 0.4$). The linear elastic properties have been used both in the linear and nonlinear FE representations.

The model was loaded with an applied displacement perpendicular to the middle of the outer surface (where the radius is R_o), while the two bases were constrained along the loading x-direction (Figure 4). The nodes at the middle of the outer surface were also constrained along the two other y- and z-directions. The reaction force at the middle nodes of the outer surface has been obtained from postprocessing. The slope of the force–displacement curve in the linear region defines the stiffness coefficient ($K = F/L$). The coefficient K has been nondimensionalized by introducing an equivalent stiffness coefficient K_{eq}. The curved honeycomb sample is assumed as a homogeneous cuboid structure with length $8H\cos(\phi)$, width $2b$, and height H_e. The
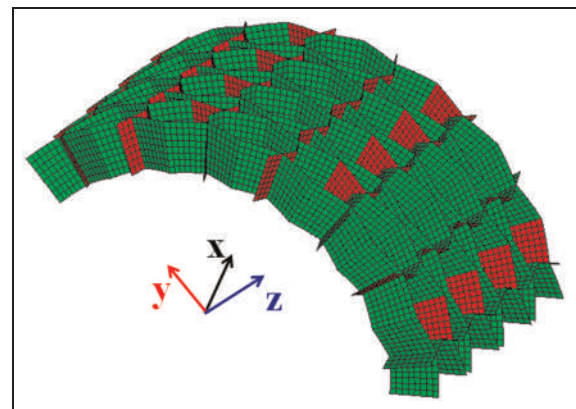

Figure 2. Full-scale finite element model of the curved SILICOMB configuration.
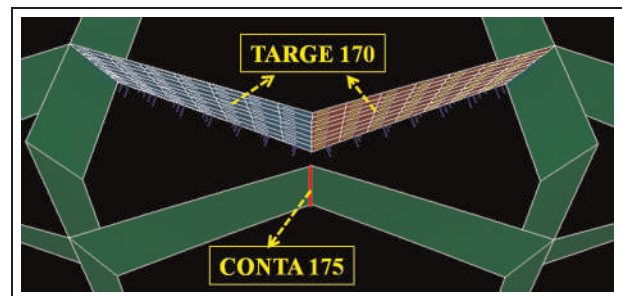

Figure 3. Example of contact pair between the nodes and surfaces.

equivalent stiffness coefficient K_{eq} is expressed based on the cuboid structure as

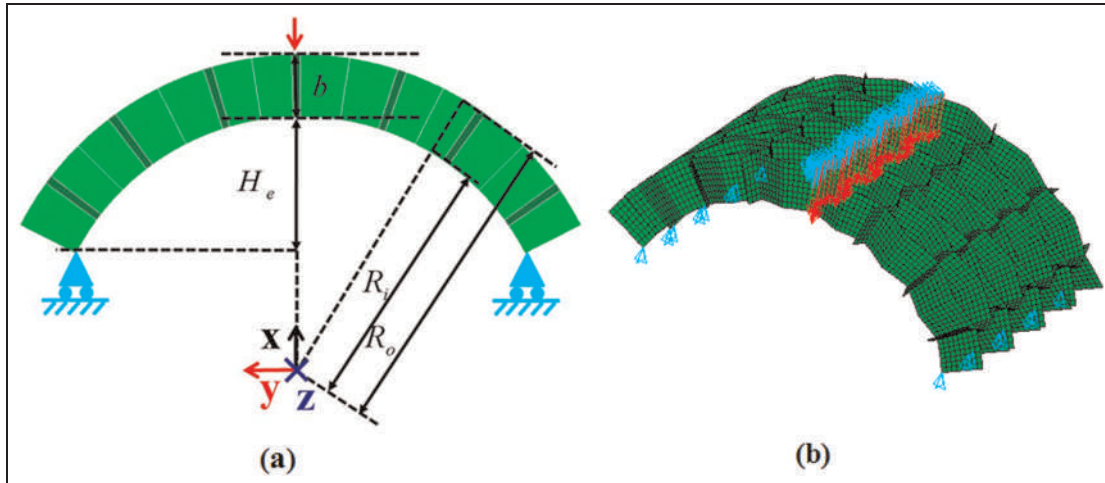$$K_{eq} = \frac{E_c A}{H_e} \tag{1}$$

Figure 4. (a) Geometry and (b) boundary conditions of the curved SILICOMB configuration.

where the symbols E_c, A, and H_e stand for the elastic modulus of the core material, the cross-sectional area, and effective height of the cuboid structure respectively. The cross-section A can be formulated as

$$A = 16Hb\cos(\phi) \quad (2)$$

Substituting equation (2) into equation (1), the expression of equivalent stiffness coefficient K_{eq} becomes

$$K_{eq} = \frac{16bHE_c\cos(\phi)}{H_e} \quad (3)$$

The relative density of the curved sample is calculated from the volume ratio of the core material V_c within a representative unit cell and the unit cell V_r

$$\frac{\rho}{\rho_c} = \frac{V_c}{V_r} \quad (4)$$

In equation (4), ρ and ρ_c represent the density of the curved cellular sample and the core material, respectively. The volumes of the core material solid and the unit cell can be calculated as

$$V_c = \left[4 \times H \times b + (R_o^2 - R_i^2) \times \varphi / \cos(\theta)\right] \times t \quad (5)$$

$$V_r = (R_o^2 - R_i^2) \times \varphi \times H \times \cos(\phi) \quad (6)$$

In equations (5) and (6), φ is the central angle of the representative unit cell and R_o and R_i are the outer and inner radii of the curved sample (Figure 1(a)). Substituting equations (5) and (6) into equation (4) and considering the nondimensional parameter expressions, the relative density can be represented as

$$\frac{\rho}{\rho_c} = \frac{\beta\left[4\alpha\gamma L^2 + (R_o^2 - R_i^2)\varphi / \cos(\theta)\right]}{\alpha(R_o^2 - R_i^2)\varphi\cos(\phi)} \quad (7)$$

Manufacturing and experimental testing

Sample manufacturing

The curved SILICOMB Kirigami cellular structure samples were manufactured using a semicrystalline thermoplastic material PEEK. APTIVE 2000 film rolls (Victrexplc, thickness: 0.25 mm) PEEK provides an interesting combination of high-temperature performance, mechanical strength, chemical resistance, and electrical insulation, as well as low moisture pick-up. The manufacturing procedure of the curved samples is made following four different steps: (a) cutting, (b) forming, (c) assembly and bonding, and (d) final curing. The rectangle and circular PEEK strips were initially obtained from the PEEK film cut using a computerized numerical control (CNC) machine (Genesis 2100, Black & White Ltd; Figure 5(a)). The rectangle PEEK strips were then placed on a rectangle aluminum mold and the edges of the strips fixed on the mold with Kapton tapes. The mold and the strips were then heated up to a temperature of 150° (the glass transition temperature of the PEEK) in a vacuum thermoforming machine (Formech FM1). To avoid residual stresses, the cooling was subsequently performed at low rate until the room temperature was reached (Figure 5(b)). In a similar way, the circular strips were thermoformed using another semicircular mold (Figure 5(c)). The third step of the manufacturing involved the bonding of the rectangle and circular strips into the final curved SILICOMB cellular structure by using two-part high-temperature epoxy glue (3M Scotch-Weld 2216 B/A Gray). The curved cellular structures were finally obtained after curing at room temperature (23°) for up to 72 h (Figure 5(d)). The geometry parameters of the curved samples produced are listed in Table 1.
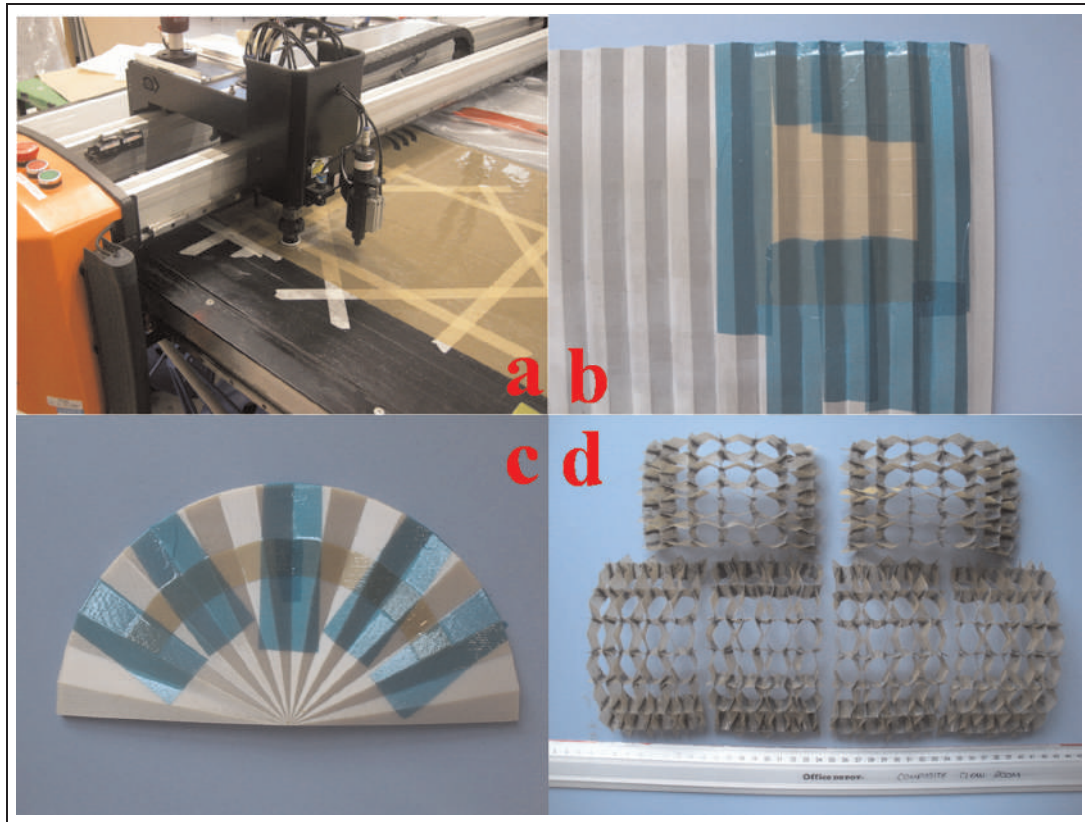
Figure 5. Manufacturing schematic diagram of curved SILICOMB sample. (a) CNC cutting of the PEEK films according to the Kirigami pattern; (b) and (c) thermoforming of the PEEK film strips in rectangular and semicircular moulds; (d) final assembled Kirigami PEEK SILICOMB samples.

Experimental testing

The stiffness coefficient of the curved SILICOMB cellular samples was measured from cyclic compression tests carried out using a materials testing machine (Instron 3343, load cell: 1 kN) with a constant displacement rate of 2 mm/min in controlled displacement mode (Figure 6). A flat steel plate was placed over the base plate of the machine to provide sufficient contact area to the support edges of the samples. In this way, the bases of the curved sample were allowed to slide horizontally on the flat steel plate, while the top of the curved cellular specimens were always in contact with the upper plate of the machine. The slight horizontal sliding of the curved sample had no observable effect on the compression deformation and the distribution of the external loading along the vertical direction. Negligible horizontal sliding was also observed during the tests. In order to increase the contact area between the bases and the flat steel plate, both bases of the curved sample were also cut to keep the contact surface with the flat steel plate as horizontal as possible (Figure 6). Therefore, the actual effective height of the samples (25 mm) is lower than the value imposed during the manufacturing. The force and displacement values were recorded using Bluehill control and acquisition software. The cyclic

Figure 6. Curved SILICOMB sample experimental setup.

Table 1. Geometry of the curved SILICOMB samples manufactured.

| Geometry	Value	Geometry	Value
Wall length L (mm)	10	Thickness of wall t (mm)	0.25
Wall length H (mm)	10	Depth of wall b (mm)	15
Angle θ (°)	20	Inner radius R_i (mm)	59.88
Angle ϕ (°)	−20	Central angle of unit cell φ (°)	35.97

tests were performed at room temperature and under controlled humidity conditions. The experimental forces versus strains are as shown in Figure 7, with each test containing four different maximum strains imposed (40%, 60%, 80%, and 100%). The strain ε has been defined as the ratio between the compression

Figure 7. Experimental cyclic compression force versus strain curves.

Figure 8. Experimental result and FE prediction curves for force versus displacement.
FE: finite element.

deformation and the effective height H_e. For increasing compression values, the force–strain curve shows a linear increase for strains lower than 0.4, followed by a nonlinear increase due to contact between the inner strips until the maximum strain is reached.

Results and discussions

Comparison between the experiments and the FE model

Figure 8 shows the comparison between the experimental results (Test 1, Test 2, and Test 3) and the FE predictions (linear, nonlinear, and transient) for strains lower than 0.4. A good agreement has been observed between the experimental result (Test #1) and the FE simulation (nonlinear and transient methods) when the displacement was lower than 6.5 mm. The nonlinear and transient FE simulations tended to provide a stiffer response beyond this displacement value because of the increased stiffness contact existing between the top nodes belonging to the internal and adjacent strips (see Figure 3). However, these pairs of nodes were not always in contact during the experiment since they were not perfectly aligned due to the manufacturing imperfections, and therefore the expected significant increase in force was not effectively taking place. The numerical loss factors (see the following paragraph for the definition of loss factor used) were also lower than the experimental ones. Against an experimental value of 0.2, the nonlinear quasi-static simulation provided a loss factor of 0.14 and the transient dynamic one of 0.17. The stabilization algorithm used during the ANSYS simulations involved the use of an energy approach to calculate the virtual equivalent viscous damping necessary for the stability, and its definition is different from the hysteretic damping calculated through the experimental curves. Moreover, a linear reduction of the damping during the load step was necessary to guarantee the numerical convergence of the solution, and this aspect also contributed to the effective decrease of the numerical loss factor. Although no complete contact between the top nodes of the samples was observed all the time, some contact friction was nevertheless occurring, an aspect not represented by the numerical simulations. All these factors concurred to produce hysteresis curves showing some
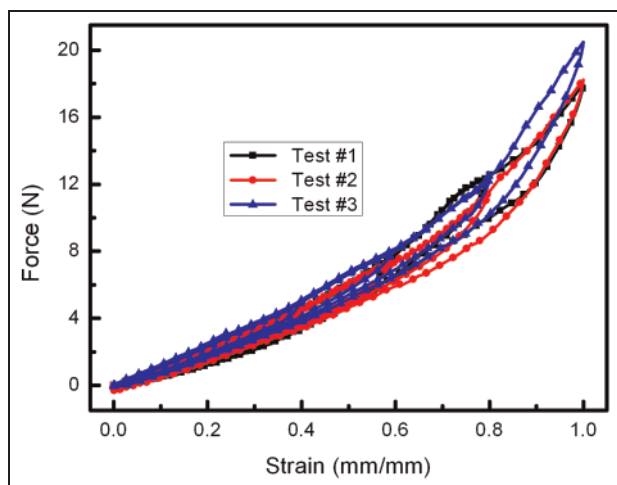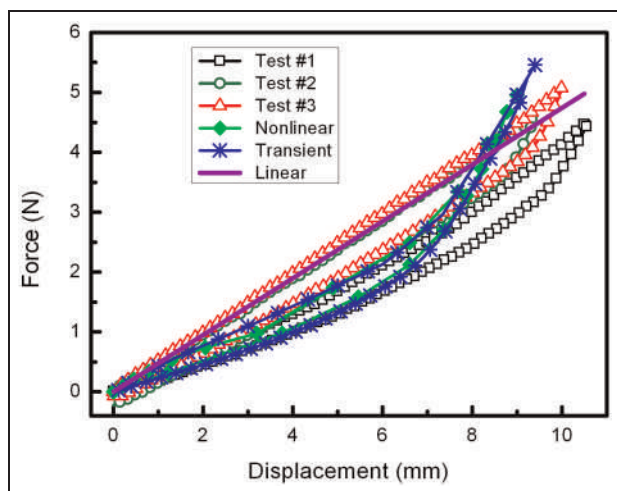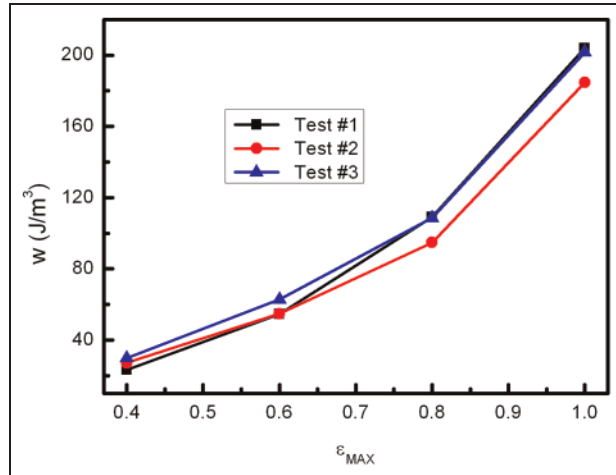
Figure 9. Experimental results for total energy absorbed per unit volume *w* versus maximum strain ε_{MAX}.

discrepancies with the experimental ones (Figure 8). However, the elastic part of the force–strain slope has been captured well by different simulations, even using the linear elastic FE model. The numerical results showed in general a slight softer response (1.5%) compared to the experimental results from Test #2. The stiffness decrease was also observed against the results from the experimental Test #3 (4.8%); however, a slightly higher stiff response (6.3%) was observed against the results from Test #1. These results provide sufficient evidence to use the elastic FE model to analyze and discuss the parametric dependence between the curved SILICOMB stiffness and the geometry parameters of the unit cell in the following sections.

Energy absorption and loss factor

Figure 9 shows the experimental results for total energy absorbed per unit volume *w* versus the maximum strain ($\varepsilon_{MAX} = 40\%, 60\%, 80\%,$ and 100%). The total energy absorbed per unit volume has been defined as

$$w = \frac{\Delta W}{V} \tag{8}$$

where ΔW and V represent the total energy absorbed and the total volume of the curved SILICOMB samples, respectively. The three tests exhibited similar trends, with an average value (in J/m^3) of the total energy absorbed per unit volume equal to 26.73 ± 3.36 for the first cycle ($\varepsilon_{MAX} = 40\%$), 57.41 ± 4.67 for the second one ($\varepsilon_{MAX} = 60\%$), 104.17 ± 8.11 for the third loop ($\varepsilon_{MAX} = 80\%$), and finally 196.69 ± 10.51 for the fourth cycle ($\varepsilon_{MAX} = 100\%$). The total energy absorbed per unit volume also showed a nonlinear increase for incremental maximum strains. The experimental results for the loss factors η versus the maximum strain ε_{MAX}

are as shown in Figure 10(a). The loss factor is calculated using the following expression

$$\eta = \frac{\Delta W}{W} \tag{9}$$

In equation (9), *W* represents the total work done on the sample. All the experimental results showed similar trends, with an average value related to the loss factor equal to 0.200 ± 0.015 for the first cycle ($\varepsilon_{MAX} = 40\%$). Other average η values were equal to 0.180 ± 0.007 for the second cycle ($\varepsilon_{MAX} = 60\%$), 0.170 ± 0.002 for the third one ($\varepsilon_{MAX} = 80\%$), and 0.185 ± 0.007 for the fourth hysteresis loop ($\varepsilon_{MAX} = 100\%$). For increasing maximum strains, the value of the loss factor tended first to decrease up to a minimum value occurring around $\varepsilon_{MAX} = 80\%$ and then to increase toward $\varepsilon_{MAX} = 1.0$. Figure 10(b) shows one hysteretic cycle curve of the experimental compression trial (Test 2). The contribution to the nonlinear hysteretic behavior provided by the contact within the inner strips is evident, with stiffening effects and contact friction characteristics.

Parametric analysis

In a similar way to planar centersymmetric reentrant configurations (Scarpa et al., 2003), SILICOMB configurations have limiting cell wall aspect ratios to avoid the opposite vertex touching each other. By inspecting Figure 1(b), it is possible to demonstrate that the following limit geometry configurations hold true

Within the red (lighter colour in black and white) dotted line

$$\alpha < \frac{2\cos(\theta)}{\sin(\phi)} \tag{10}$$

Within the blue (darker colour in black and white) dotted line

$$\alpha > \frac{2\sin(\theta)}{\cos(\phi)} \tag{11}$$

Figure 11 shows the values of α (H/L) versus the angle ϕ for different internal angles θ. In this study, the range of the internal cell angles ϕ and θ is within 5° and 85°. For increasing ϕ angles, the corresponding upper bound value of α decreases from 22.86 to 2, while the lower bound increases from 0.18 to 2 for $\theta = 5°$. Similarly, the upper bound for α decreases from 20.80 to 1.82 (16.23 to 1.42, 9.70 to 0.85, and 2 to 0.18) when the angle θ is parameterized between 25°, 45°, 65°, and 85°. On the contrary, the lower bound value of α increases from 0.85 to 9.70 (1.42 to 16.23, 1.82 to 20.80, and 2 to 22.86) for the same set of θ values. In this study, the value of α is limited between an upper bound of 5.50 and a lower bound of 0.73 for internal cell angles $\theta = 20°$ and $\phi = -20°$.
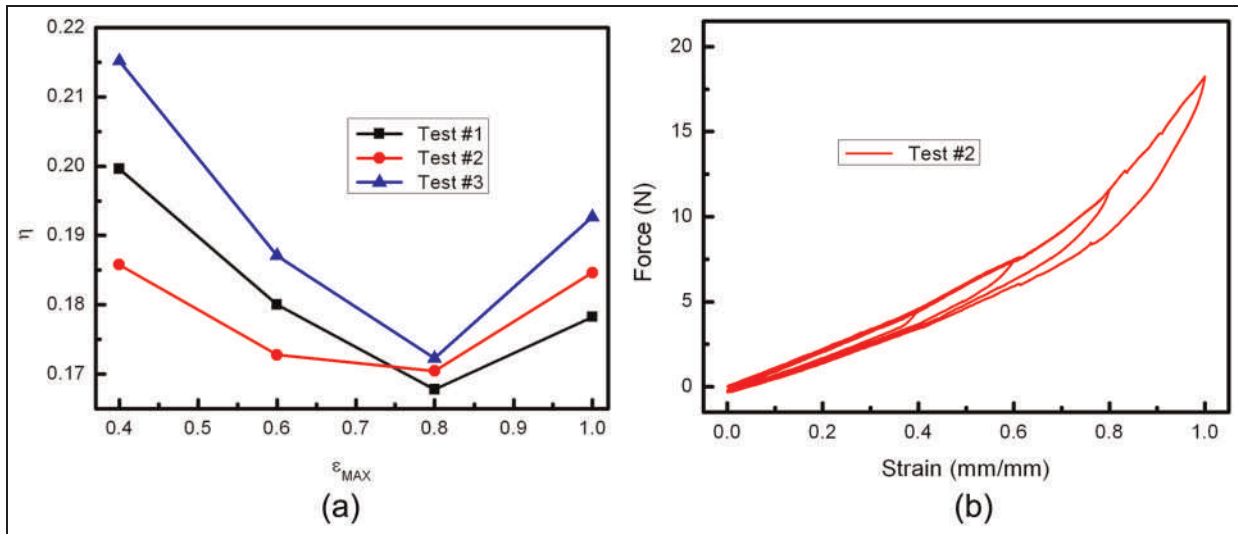
Journal of Intelligent Material Systems and Structures 25(6)

Figure 10. Experimental results curves: (a) loss factor η versus maximum strain ε_{MAX} and (b) compression force versus strain.

Figures 12 and 13 show the variation of the stiffness coefficient versus different geometry parameters of the curved cellular topology. All the results are referred to the baseline configuration of 3.5 × 4 cells used for the manufactured samples. The same curvature radius ($R = (R_o + R_i)/2$) has been considered during the parametric analysis. The figures show results related to the variation of one or two geometry parameters, while the others are kept constant. The baseline geometry parameters are illustrated in Table 1. Figure 12(a) shows the behavior of the nondimensional stiffness coefficient K/K_{eq} versus the nondimensional curvature R/L for different wall lengths L. At increasing R/L values, the nondimensional stiffness coefficient decreases when L is kept constant. On the contrary, K/K_{eq} decreases for

increasing L values. The variations of the nondimensional stiffness coefficient versus R/L at different aspect ratios $\alpha = H/L$ are as shown in Figure 12(b). For increasing R/L values, the parameter K/K_{eq} decreases when α is kept constant. The magnitude of the nondimensional stiffness also decreases for higher values of cell wall aspect ratio.

The sensitivity of the nondimensional stiffness versus the nondimensional curvature for different thickness ratios $\beta = t/L$ is as shown in Figure 12(c). It is possible to also observe in this case the pattern of a decreasing stiffness coefficient for increasing R/L values and a stiffening effect of the mechanical performance of the cellular core for increasing β. The increase in the nondimensional stiffness for the curved cellular configuration for increasing thickness values is compatible with the stiffening effect provided in planar and prismatic centersymmetric honeycomb cells when the thickness of the walls is increased (Gibson and Ashby, 1997). Aside from the quasi-inverse dependence versus R/L observed also for the other parametric analysis, the stiffness appears to increase with the depth ratio $\gamma = b/L$ (Figure 12(d)). This is an interesting phenomenon, because in planar hexagonal structures the through-the-thickness stiffness is dependent on the relative density only (Gibson and Ashby, 1997), while the transverse shear in the plane (yz) tends to approach a lower bound, the other (xz) is dependent on the unit cell geometry only and not on the depth ratio (Scarpa and Tomlin, 2000). A similar behavior has also been observed in SILICOMB planar honeycomb structures, although the dependence of the transverse shear modulus G_{yz} versus γ is far less marked than in centersymmetric hexagonal honeycombs (Lira et al., 2011). The curved geometry of the cellular structure appeared to
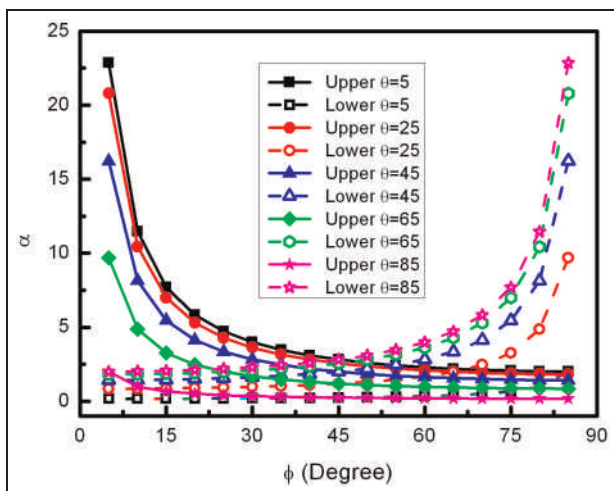

Figure 11. Permissible ranges of α values (H/L) versus angle ϕ with different constant θ angles.
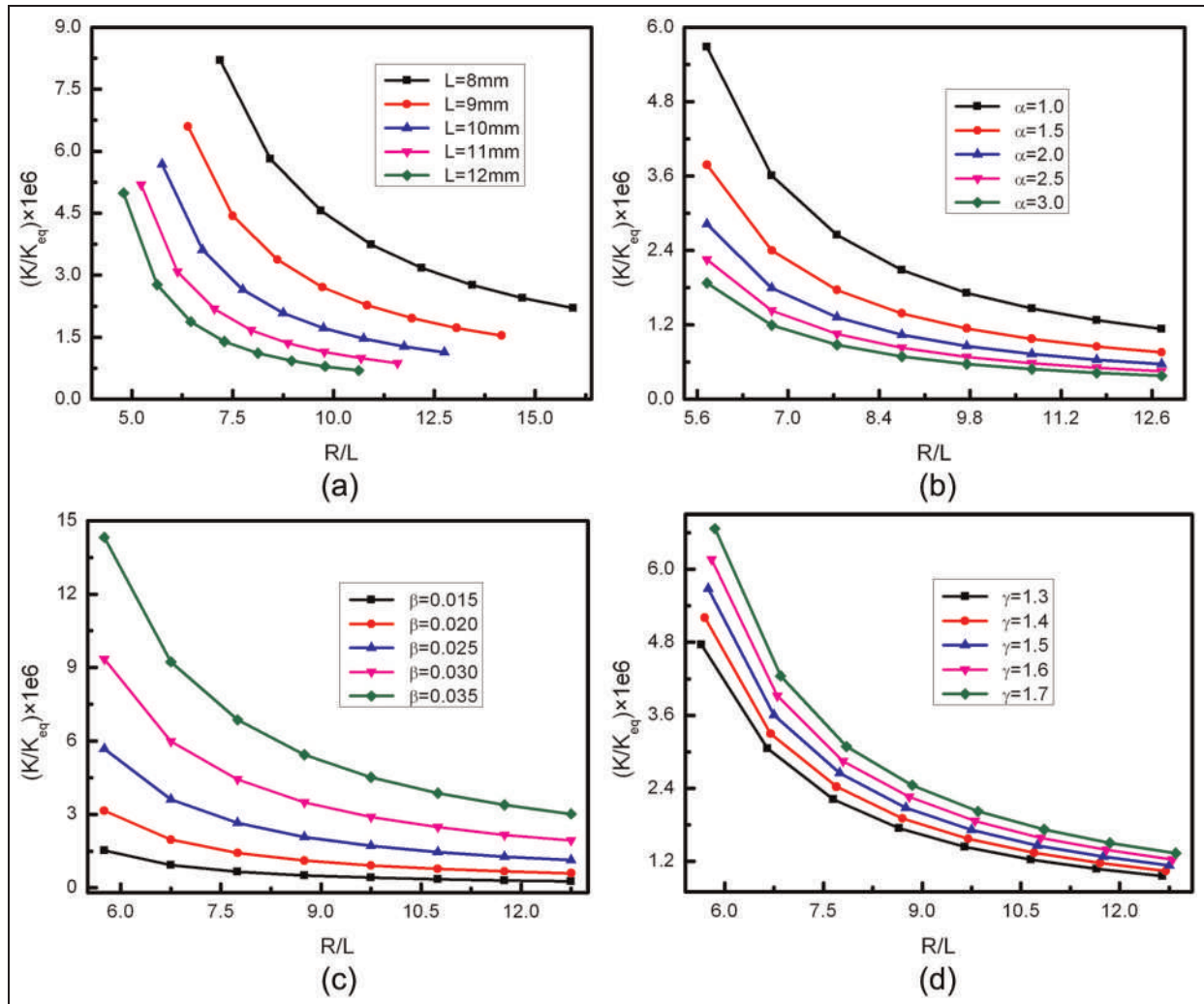
Figure 12. FE prediction of the nondimensional stiffness coefficient (K/K_{eq}) versus curvature radius (R/L): (a) for different wall lengths (L); (b) for different cell wall aspect ratios ($\alpha = H/L$); (c) for different thickness ratios ($\beta = t/L$); and (d) for different depth ratios ($\gamma = b/L$).
FE: finite element.

have created equivalent hoop stresses during the three-point bending simulation, therefore providing an increase in the nondimensional stiffness coefficient, even more marked for thicker honeycomb sections.

The dependence of the nondimensional stiffness coefficient versus the internal angle θ for different R/L values can be observed in Figure 13(a). When the nondimensional curvature R/L is constant, K/K_{eq} presents a symmetric behavior between $\theta = -20°$ and $\theta = 20°$, with a maximum value occurring at $\theta = 0°$. A similar behavior has been observed for the E_x modulus in planar SILICOMB configurations (Lira et al., 2009). The use of decreasing nondimensional curvatures R/L did contribute to the increase in the stiffness. The behavior of the nondimensional stiffness is opposite to the one recorded for the dependence versus θ, when both the nondimensional curvature and the angle ϕ are considered (Figure 13(b)). K/K_{eq} reaches a minimum for

$\phi = 0$, and the stiffness tends to decrease for increasing R/L values. Planar SILICOMB structures also exhibit a minimum for the in-plane Young's modulus when φ is varied between $-20°$ and $20°$ (Lira et al., 2009).

Density is an important design parameter when selecting core materials in lightweight sandwich applications. The carpet plot in Figure 14(a) illustrates the dependence of K/K_{eq} versus the relative density ρ/ρ_c for different wall lengths L and different curvature radii R/L. For increasing relative density, K/K_{eq} tends to decrease when L is kept constant. On the contrary, the nondimensional stiffness increases when the R/L value is fixed. A similar trend has also been observed for the nondimensional stiffness coefficient K/K_{eq} was varied against the relative density with different aspect ratios and different nondimensional curvatures (Figure 14(b)). For increasing ρ/ρ_c, K/K_{eq} decreases when α is kept constant, but increases with the relative density with a
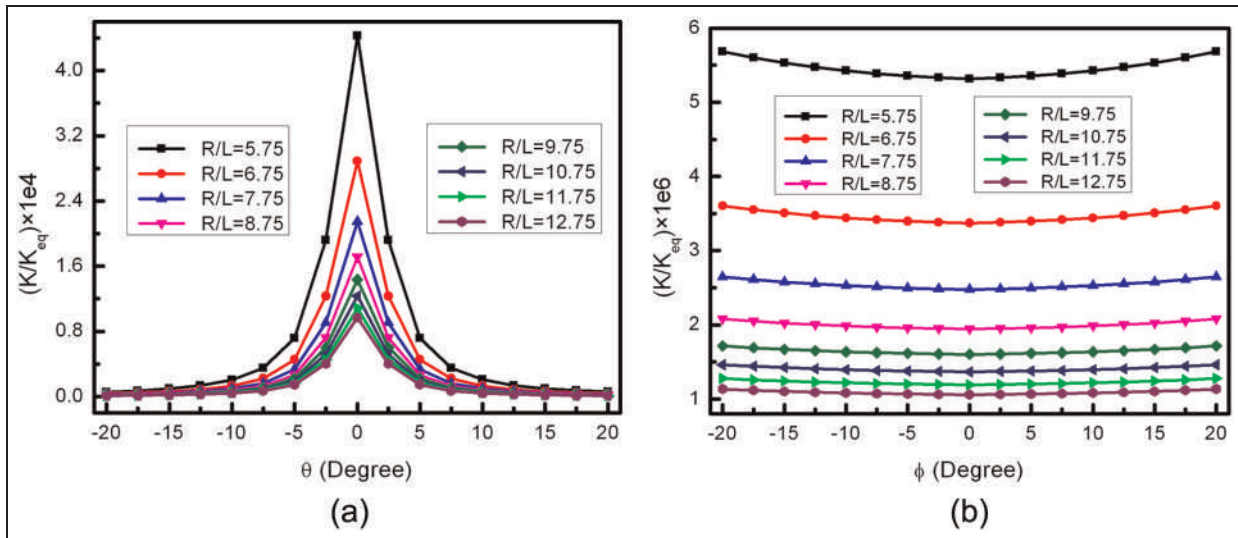
Figure 13. Nondimensional stiffness coefficient (K/K_{eq}) versus angle values for different curvature radii (R/L): (a) angle (θ) and (b) angle (ϕ).

clear linear trend when R/L is kept constant. Moreover, for increasing ρ/ρ_c values K/K_{eq} exhibits a marked decrease when β is constant, while the opposite is true when R/L values are fixed (Figure 14(c)). An increase in the relative density by a factor of 2.3 leads to a stiffness increase of 9.3 times for $R/L = 5.75$. A different type of behavior has been observed in the carpet plot illustrating the dependence of K/K_{eq} versus ρ/ρ_c for different depth ratios $\gamma = b/L$ and different R/L values (Figure 14(d)). For increasing ρ/ρ_c values, K/K_{eq} shows a decrease when γ and R/L are kept constant. If ρ/ρ_c is fixed, the nondimensional stiffness shows a significant increase for decreasing γ and R/L values. As an example, when the relative density is 4.09%, K/K_{eq} increases by 42.3% when γ passes from 1.7 to 1.3 and for R/L passing from 7.75 to 5.75. The nondimensional stiffness tends to decrease for relative densities ranging between 3.8% and 4.1% and increasing internal cell angle θ values. At constant ρ/ρ_c, the nondimensional stiffness shows an increase for lower R/L values (Figure 14(e)). A different behavior is, however, observed from the carpet plot representing K/K_{eq} versus the relative density at different angles ϕ and different R/L values (Figure 14(f)). Increases in the relative density show very slight augmentation of the nondimensional stiffness at R/L constant; on the contrary, K/K_{eq} tends to decrease significantly when ϕ is fixed. At constant values of ρ/ρ_c, K/K_{eq} tends to provide higher values for decreasing R/L, but features higher magnitudes at higher ϕ angles.

The effective height H_e is another parameter to be considered for engineering applications since it can be used to determine the maximum compression deformation (Figure 4 (a)). The nondimensional effective height H_e/R versus R/L is as shown in Figure 15(a) for

different wall lengths L. At increasing R/L values, the H_e/R parameter tends to lower its magnitude at L constant, showing dependence close to $(R/L)^{-1}$. No significant sensitivity about the nondimensional height versus R/L was found for different values of L. A dissimilar type of behavior is, however, observed when the nondimensional height is parameterized against the internal cell angle θ and different nondimensional curvature values R/L (Figure 15(b)). When R/L is constant, the nondimensional height assumes the same value at $\theta = -20°$ and $\theta = 20°$, with a symmetric distribution around $\theta = 0°$ for which H_e/R reaches its maximum value. High values of R/L tend to decrease the nondimensional height at θ constant by a factor of 4.7 when R/L is increased from 5.75 to 12.75, showing a strong sensitivity of the H_e/R parameter against the radius of the curved SILICOMB structure.

Conclusion

In this work, a novel curved cellular structure has been produced using Kirigami techniques from PEEK films and has been investigated from a numerical and experimental point of view. The focus of the analysis was about the possible relation between the stiffness of the curved cellular structure and the geometry parameters of its representative unit cell. The fidelity of the FE full-scale models used has been validated by the experimental results. A parametric analysis has shown that it is possible to obtain significant variations of the stiffness by intervening on the geometry parameters of the curved sample. The analysis also suggested the possibility of using curved SILICOMB configuration to design core structures with minimum density and maximum stiffness coefficients. Experimental evidence also
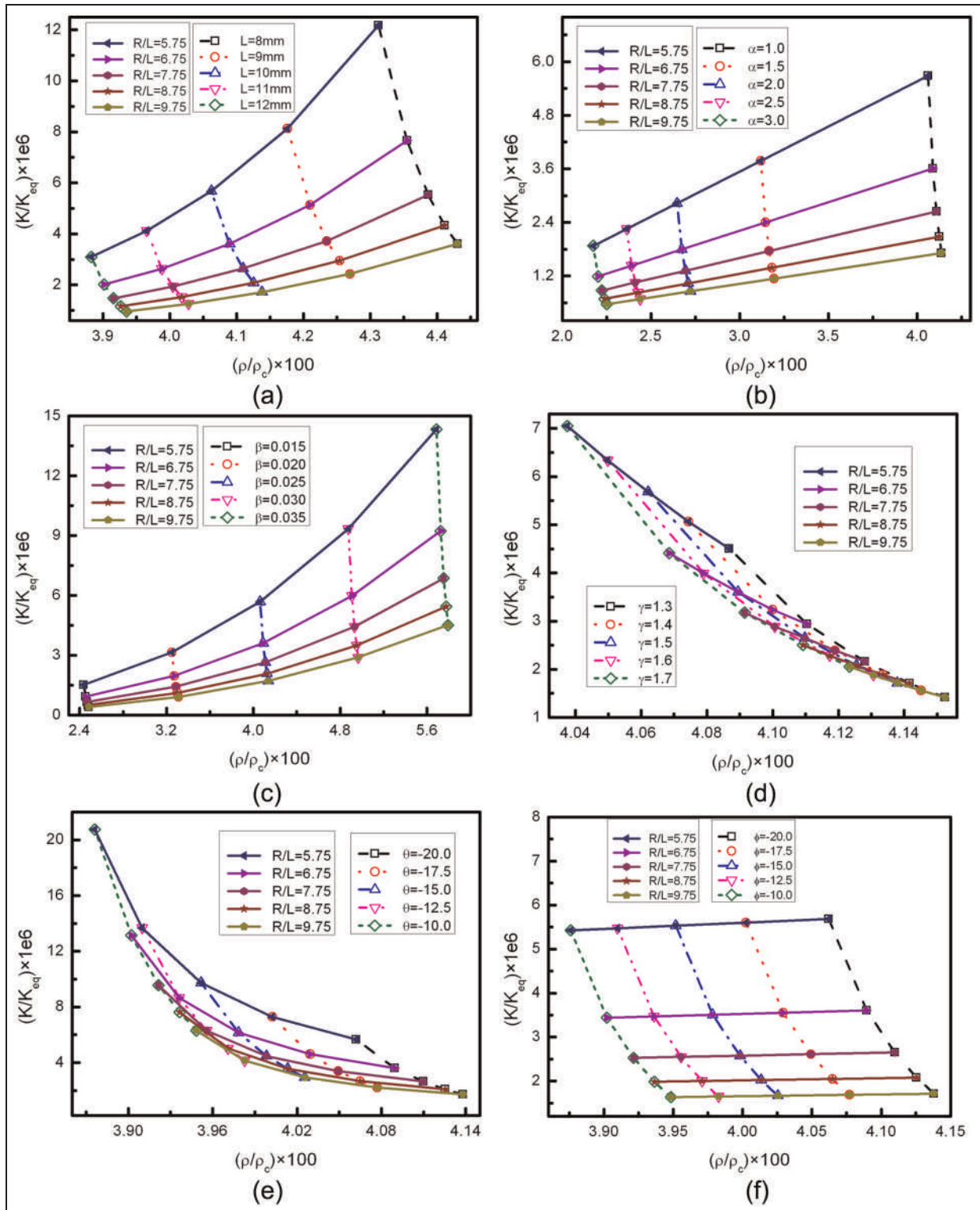
Figure 14. Nondimensional stiffness coefficient (K/K_{eq}) versus relative density (ρ/ρ_c) for different R/L values with (a) different wall lengths L; (b) different aspect ratios α; (c) different thicknesses ratios β; (d) different depth ratios γ; (e) different angles θ; and (f) different angles ϕ.

showed that general strain dependence could be observed in the energy absorption capability and loss factors of the curved samples. The large deformation

capability with good shape recovery shown by the curved PEEK SILICOMB samples coupled with the tailoring of the mechanical properties suggest the
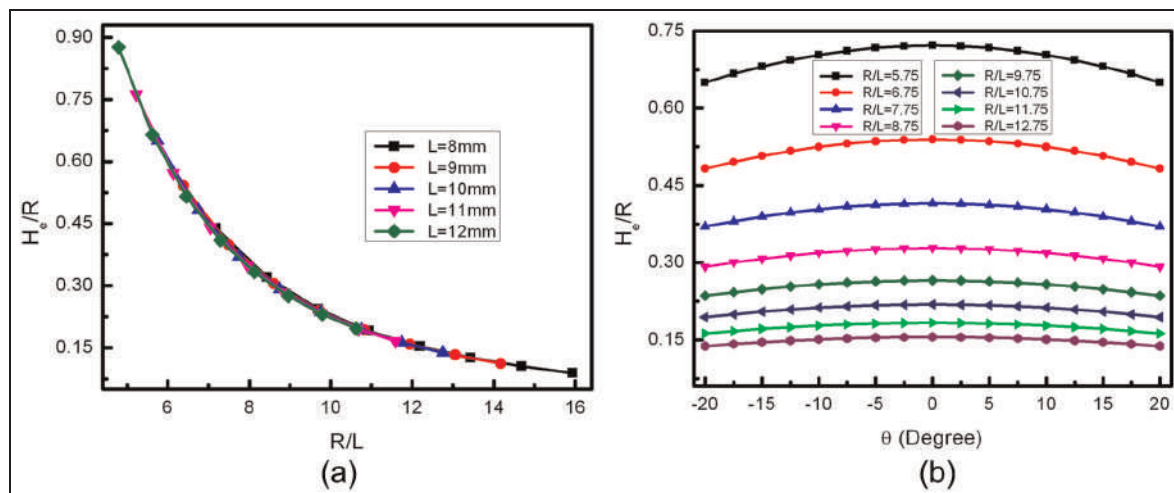
Figure 15. Relation between the effective height and the unit cell geometry parameters: (a) H_e/R versus R/L at different L values and (b) H_e/R versus angle θ for different R/L values.

potential use of these cellular structures at ZPR for shape morphing applications.

Declaration of conflicting interests

The authors declare that there is no conflict of interest.

References

Alderson A, Alderson K, Attard D, et al. (2010a) Elastic constants of 3-, 4-and 6-connected chiral and anti-chiral honeycombs subject to uniaxial in-plane loading. *Composites Science and Technology* 70: 1042–1048.

Alderson A, Alderson K, Chirima G, et al. (2010b) The in-plane linear elastic constants and out-of-plane bending of 3-coordinated ligament and cylinder-ligament honeycombs. *Composites Science and Technology* 70: 1034–1041.

Bettini P, Airoldi A, Sala G, et al. (2010) Composite chiral structures for morphing airfoils: numerical analyses and development of a manufacturing process. *Composites Part B: Engineering* 41: 133–147.

Bezazi A, Scarpa F and Remillat C (2005) A novel centresymmetric honeycomb composite structure. *Composite Structures* 71: 356–364.

Bitzer T (1997) *Honeycomb Technology: Materials, Design, Manufacturing, Applications and Testing*. London: Chapman & Hall.

Bornengo D, Scarpa F and Remillat C (2005) Evaluation of hexagonal chiral structure for morphing airfoil concept. *Proceedings of the Institution of Mechanical Engineers, Part G: Journal of Aerospace Engineering* 219: 185–192.

Bubert EA, Woods BKS, Lee K, et al. (2010) Design and fabrication of a passive 1D morphing aircraft skin. *Journal of Intelligent Material Systems and Structures* 21: 1699–1717.

Engelmayr GC, Cheng M, Bettinger CJ, et al. (2008) Accordion-like honeycombs for tissue engineering of cardiac anisotropy. *Nature Materials* 7: 1003–1010.

European Project M-RECT. Available at: http://cordis.europa.eu/projects/rcn/94838_en.html

Evans K (1991) The design of doubly curved sandwich panels with honeycomb cores. *Composite Structures* 17: 95–111.

Evans K and Alderson K (2000a) Auxetic materials: the positive side of being negative. *Engineering Science and Education Journal* 9: 148–154.

Evans KE and Alderson A (2000b) Auxetic materials: functional materials and structures from lateral thinking! *Advanced Materials* 12: 617–628.

Gibson LJ and Ashby MF (1997) *Cellular Solids: Structure and Properties*. 2nd ed. Cambridge University Press, Cambridge, UK.

Grima JN, Oliveri L, Attard D, et al. (2010) Hexagonal honeycombs with zero Poisson's ratios and enhanced stiffness. *Advanced Engineering Materials* 12: 855–862.

Hassan M, Scarpa F, Ruzzene M, et al. (2008) Smart shape memory alloy chiral honeycomb. *Materials Science and Engineering: A* 481: 654–657.

Jeong SM and Ruzzene M (2004) Analysis of vibration and wave propagation in cylindrical grid-like structures. *Shock and Vibration* 11: 311–332.

Lakes R (1987) Foam structures with a negative Poisson's ratio. *Science* 235: 1038–1040.

Lira C, Scarpa F, Olszewska M, et al. (2009) The SILICOMB cellular structure: mechanical and dielectric properties. *physica status solidi (b)* 246: 2055–2062.

Lira C, Scarpa F, Tai Y, et al. (2011) Transverse shear modulus of SILICOMB cellular structures. *Composites Science and Technology* 71: 1236–1241.

Martin J, Heyder-Bruckner JJ, Remillat C, et al. (2008) The hexachiral prismatic wingbox concept. *physica status solidi (b)* 245: 570–577.

Masters I and Evans K (1996) Models for the elastic deformation of honeycombs. *Composite Structures* 35: 403–422.

Miller W, Smith C, Scarpa F, et al. (2010) Flatwise buckling optimization of hexachiral and tetrachiral honeycombs. *Composites Science and Technology* 70: 1049–1056.

Milton GW (1992) Composite materials with Poisson's ratios close to—1. *Journal of the Mechanics and Physics of Solids* 40: 1105–1137.

Olympio KR and Gandhi F (2007) Zero-ν cellular honeycomb flexible skins for one-dimensional wing morphing. In: *Proceedings of the 48th AIAA/ASME/ASCE/AHS/ASC structures, structural dynamics, and materials conference*, Honolulu, HI, 23–26 April.

Olympio KR and Gandhi F (2010a) Flexible skins for morphing aircraft using cellular honeycomb cores. *Journal of Intelligent Material Systems and Structures* 21: 1719–1735.

Olympio KR and Gandhi F (2010b) Zero Poisson's ratio cellular honeycombs for flex skins undergoing one-dimensional morphing. *Journal of Intelligent Material Systems and Structures* 21: 1737–1753.

Saito K, Agnese F and Scarpa F (2011) A cellular Kirigami morphing wingbox concept. *Journal of Intelligent Material Systems and Structures* 22: 935–944.

Scarpa F and Tomlin P (2000) On the transverse shear modulus of negative Poisson's ratio honeycomb structures. *Fatigue & Fracture of Engineering Materials & Structures* 23: 717–720.

Scarpa F, Smith C, Ruzzene M, et al. (2008) Mechanical properties of auxetic tubular truss-like structures. *physica status solidi (b)* 245: 584–590.

Scarpa F, Smith F, Chambers B, et al. (2003) Mechanical and electromagnetic behaviour of auxetic honeycomb structures. *Aeronautical Journal* 107: 175–183.

Spadoni A, Ruzzene M and Scarpa F (2006) Dynamic response of chiral truss-core assemblies. *Journal of Intelligent Material Systems and Structures* 17: 941–952.